PCCP

PAPER

View Article Online
View Journal | View Issue

Check for updates

Cite this: *Phys. Chem. Chem. Phys.*, 2017, **19**, 9790

Probing the bonding of CO to heteronuclear group 4 metal–nickel clusters by photoelectron spectroscopy†

Jinghan Zou,‡[ab] Hua Xie,‡[a] Qinqin Yuan,[ab] Jumei Zhang,[ab] Dongxu Dai,[a] Hongjun Fan,[a] Zichao Tang[c] and Ling Jiang *[a]

Received 10th January 2017, Accepted 11th March 2017

DOI: 10.1039/c7cp00171a

rsc.li/pccp

A series of heterobinuclear group 4 metal–nickel carbonyls $MNi(CO)_n^-$ (M = Ti, Zr, Hf; n = 3–7) has been generated *via* a laser vaporization supersonic cluster source and characterized by mass-selected photoelectron velocity-map imaging spectroscopy. Quantum chemical calculations have been carried out to elucidate the geometric and electronic structures and support the spectral assignments. The n = 3 cluster is determined to be capable of simultaneously accommodating three different types of CO bonds (*i.e.*, side-on-bonded, bridging, and terminal modes), resulting in a $MNi[\eta^2(\mu_2\text{-C, O})](\mu\text{-CO})(CO)^-$ structure, which represents the smallest metal carbonyl with the involvement of all the main modes of metal–CO coordination to date. The building block of three bridging CO molecules is favored at n = 4, the structure of which persists up to n = 7. The additional CO ligands are bonded terminally to the metal atoms. The present findings provide important new insight into the structure and bonding mechanisms of CO molecules with heteronuclear transition metals, which would have important implications for understanding chemisorbed CO molecules on alloy surfaces.

1. Introduction

The interaction of carbon monoxide with transition metals is of considerable interest due to its importance in heterogeneous and homogeneous catalysis such as Fischer–Tropsch chemistry, hydroformylation, alcohol synthesis, and acetic acid synthesis.[1] Considering that a high dispersion leads to an increase in the activity because of the maximization of the active surface, qualitatively novel chemical properties would emerge for clusters and nanosized particles.[2] Metal clusters are often regarded as models for the surface of bulk materials, which provide a nice correlation with the elemental reactions on the most active or least coordinated site of a catalyst.[3] Particularly, transition metal carbonyls afford a prototypical system for the investigation of the structure and bonding of CO with metals. CO is well known to coordinate in the direction from the C atom to metal(s), forming terminal or bridging metal–CO bonding, in the metal carbonyls with very few exceptions for chemisorbed CO on some transition metal surfaces[4–6] and the so-called "four-electron donor" CO in a limited number of organometallic complexes.[7–9]

Mononuclear metal carbonyls have been extensively explored by various types of experimental and theoretical methods.[10–15] Recently, the study of binuclear metal carbonyls has gained increasing interest, which serves as the smallest model for the bonding of CO to metal clusters. $Cu_2(CO)_6^+$ has an unbridged D_{3d} structure with a Cu–Cu half bond, in which CO is terminally bonded to the copper atoms.[16] In the $Au_6(CO)_n^-$ (n = 0–3) carbonyls, the first three CO terminally chemisorb to the three apex sites of the D_{3h} Au_6, which has little effect on the electron binding energies.[17] Photoelectron spectroscopy of $Ni_n(CO)_m^-$ and $Pt_n(CO)_m^-$ has shown that the saturation with CO on the bare metal cluster is due to the formation of an electronic closed shell.[18] $Co_2(CO)_6^+$ was identified to be the coordination-saturated cluster for Co_2^+, which was characterized to have C_s symmetry involving a bridging CO ligand and a Co–Co single bond.[19] Infrared multiple photon dissociation spectroscopy of rhodium carbonyls has shown that the neutral $Rh_2(CO)_8$ complex has two bridging CO and six terminal CO groups, whereas all CO molecules are terminally bonded in the cationic

---

[a] *State Key Laboratory of Molecular Reaction Dynamics, Collaborative Innovation Center of Chemistry for Energy and Materials (iChEM), Dalian Institute of Chemical Physics, Chinese Academy of Sciences, 457 Zhongshan Road, Dalian 116023, Liaoning, P. R. China. E-mail: ljiang@dicp.ac.cn*

[b] *University of Chinese Academy of Sciences, 19A Yuquan Road, Beijing 100049, P. R. China*

[c] *State Key Laboratory of Physical Chemistry of Solid Surfaces, Department of Chemistry, College of Chemistry and Chemical Engineering, Xiamen University, Xiamen 361005, P. R. China*

† Electronic supplementary information (ESI) available: Comparison of experimental and calculated results for $MNi(CO)_n^-$ (M = Zr, Hf; n = 3–7) (Tables S1 and S2); time-of-flight mass spectrum of $TiNi(CO)_n^-$ (Fig. S1); optimized structures of $MNi(CO)_n^-$ (M = Zr, Hf; n = 3–7) (Fig. S2 and S3). See DOI: 10.1039/c7cp00171a

‡ These authors contributed equally to this work.

$Rh_2(CO)_8^+$ complex.[20] The $Fe_2(CO)_8^-$, $Fe_2(CO)_8^+$, and $Fe_2(CO)_9^+$ complexes were characterized to have unbridged structures.[21–23] The $Cr_2(CO)_n^+$ clusters consist of $(OC)_5Cr–C–O–Cr(CO)_{n-6}^+$ with a linear bridging carbonyl group bonded to one chromium atom through its carbon atom and to the other chromium atom through its oxygen atom.[24] In the $Ti_2(CO)_n^-$ (n = 1–9) series, the CO molecules bind to Ti_2 in a side-on-bonded fashion and form a stable $Ti_2[\eta^2(\mu_2\text{-C, O})]_3$ structure at n = 3. The motif of this structure retains up to n = 5 and starting at n = 6, a new building block of two CO groups side-on-bonded to Ti_2 is favored, the structure of which persists up to n = 9.[25]

In contrast, few efforts have been made for heterobinuclear metal carbonyls. The carbonyl groups are found to bond terminally to the nickel atom in the $CuNi(CO)_3^-$ cluster or the iron atom in the $CuFe(CO)_4^-$ and $PbFe(CO)_4^-$ clusters.[26–28] The $MFe(CO)_8^+$ (M = Co, Ni, Cu) complexes consist of eclipsed $(CO)_5Fe–M(CO)_3^+$ structures and $MCu(CO)_7^+$ (M = Co, Ni) have staggered $(CO)_4M–Cu(CO)_3^+$ structures, in which all the CO molecules are terminally bonded to the metal atoms.[29] In the heterobinuclear main group metal–nickel carbonyls $MNi(CO)_3^-$ (M = Mg, Ca, Al), the three carbonyls are only terminally bonded to the nickel atom, resulting in the formation of the $Ni(CO)_3$ motif.[30]

There has been no report thus far of a simple tricarbonyl compound in which the three types of typical metal–CO coordination of side-on-bonded, bridging, and terminal carbonyls are simultaneously involved. Herein, we report a photoelectron velocity-map imaging spectroscopic and theoretical study of mass-selected heterobinuclear group 4 metal–nickel carbonyl cluster anions, $MNi(CO)_n^-$ (M = Ti, Zr, Hf; n = 3–7). The n = 3 cluster is determined to be capable of simultaneously accommodating three different types of CO bonding (*i.e.*, side-on-bonded, bridging, and terminal modes), resulting in the formation of a $MNi[\eta^2(\mu_2\text{-C, O})](\mu\text{-CO})(CO)^-$ structure, which represents the smallest metal carbonyl with the involvement of all the main modes of metal–CO coordination to date. The building block of three bridging CO molecules is favored at n = 4, the structure of which persists up to n = 7.

2. Experimental

The experiment was carried out using a homemade instrument with a laser vaporization source, a dual-channel time-of-flight mass spectrometer (D-TOFMS) coupled with velocity-map photoelectron imaging analyzer. Details of the apparatus have been described elsewhere,[31] and only a brief outline is given below. The heterodinuclear transition metal carbonyl anions were produced from the laser vaporization process in a supersonic expansion of helium gas seeded with 5% CO. A pulsed general valve (Series 9) was employed for the introduction of gas. The typical stagnation pressure of the carrier gas was about 2–3 atm. The second harmonic of a Nd:YAG laser (Continuum, Minilite II) was used to vaporize the rotating alloy targets. The cluster anions were cooled and expanded into the source chamber. These anionic clusters were mass selected by a McLaren Wiley time-of-flight spectrometer and then crossed with a laser beam in the photodetachment region. The photon energies of 355 nm (3.496 eV) and 532 nm (2.331 eV) were used for the photodetachment of these anionic clusters. The resulting photoelectrons were extracted by a velocity map imaging photoelectron spectrometer and recorded by a charge-coupled device camera. Each image was obtained with 10 000–50 000 laser shots at 10 Hz repetition rate. The final raw image stands for the projection of the photoelectron density in the 3D laboratory frame onto the 2D imaging detector. The original 3D distribution was reconstructed using the Basis Set Expansion (BASEX) inverse Abel transform method, and the photoelectron spectrum was acquired. The photoelectron kinetic energy spectra were calibrated by the known spectrum of Au^-. The energy resolution was better than 5%, corresponding to 50 meV at an electron kinetic energy (eKE) of 1 eV.

3. Theoretical details

In order to interpret the geometrical and electronic structures of $MNi(CO)_n^{0/-1}$ (M = Ti, Zr, Hf), theoretical computations were carried out using the Gaussian 09 programs.[32] Recent investigations have shown that the BP86 function worked well for the titanium carbonyls,[25,33] and then it was employed here. The Aug-cc-pVTZ basis set was selected for the C and O atoms, and the SDD (SC-RECP, MWB28) basis set was used for the Ti, Zr, Hf, and Ni atoms. Vibration analysis was implemented to make sure that the obtained structures were real minima on the potential energy surfaces. Theoretically, the vertical detachment energy (VDE) was computed as the difference in energy between the neutral and anionic species based on the optimized anion geometry, and the adiabatic detachment energy (ADE) was calculated as the difference in energy between the neutral and the anion species both at their optimized geometries.

4. Results and analysis

4.1 Photoelectron spectroscopy

The $MNi(CO)_n^-$ (M = Ti, Zr, Hf) complexes were generated *via* laser vaporization of metal rods with 5% CO seeded in helium. The typical mass spectrum of titanium–nickel carbonyl cluster anions is shown in Fig. S1 in the ESI.† In addition to the $TiNi(CO)_n^-$ (n = 3–7) target products, the $Ni(CO)_3^-$, $Ti_2(CO)_n^-$ (n = 4–6), and $Ni_2(CO)_n^-$ (n = 4–6) complexes were also observed. The carbonyl anions of interest were mass-selected and introduced into the photodetachment region. The photoelectron imaging results and corresponding photoelectron spectra of $TiNi(CO)_n^-$ (n = 3–7) are shown in Fig. 1, and those of $ZrNi(CO)_n^-$ and $HfNi(CO)_n^-$ (n = 3–5) are depicted in Fig. 2 and 3, respectively.

For $TiNi(CO)_n^-$, the single photon energy of 355 nm (3.496 eV) allowed ground state transitions of all compounds to be observed, as shown in Fig. 1. The 532 nm (2.331 eV) spectrum was successfully measured for $TiNi(CO)_3^-$ (see the inset in Fig. 1), but not for $TiNi(CO)_n^-$ (n = 4–7), indicating that the photon energy of 532 nm was not sufficient for the photodetachment of larger clusters. In the 532 nm spectrum of $TiNi(CO)_3^-$, energy separation between the two peaks of the X band was measured to be 2016 cm^{-1}, which

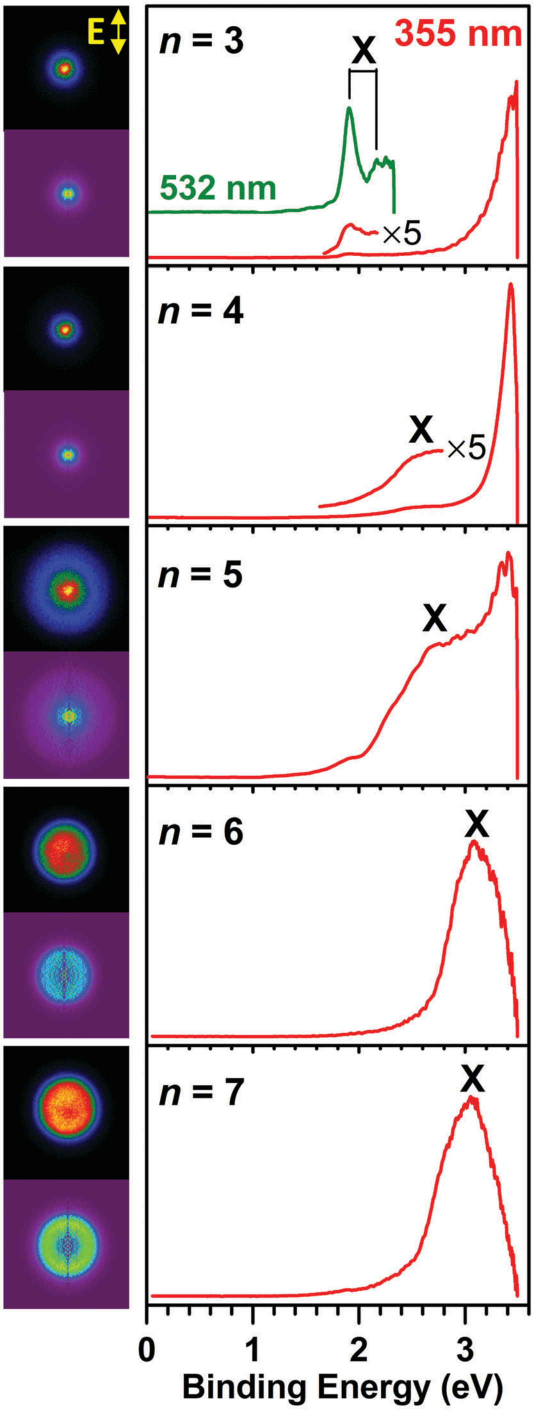

Fig. 1 Photoelectron images of $TiNi(CO)_n^-$ (n = 3–7) at 355 nm. The photoelectron spectrum of $TiNi(CO)_3^-$ at 532 nm is depicted in the embedded figure. The raw image (upper) and the reconstructed image (bottom) after inverse Abel transformation are shown on the left side. The double arrow indicates the direction of the laser polarization. Photoelectron spectra are shown on the right side. Vibrational progression of the ground state is indicated with vertical lines for n = 3.

is characteristic of vibrational frequency of terminal CO. The VDE values of $TiNi(CO)_n^-$ (n = 3–7) were estimated from their X band maxima in the 355 nm spectra to be 1.93 ± 0.08, 2.56 ± 0.05, 2.98 ± 0.03, 3.05 ± 0.02, and 3.10 ± 0.02 eV (Table 1), respectively.

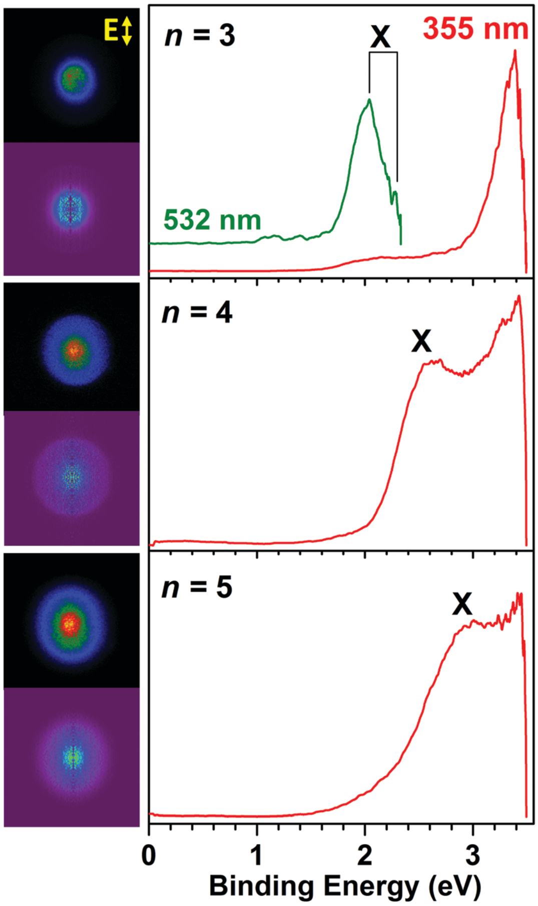

Fig. 2 Photoelectron images of $ZrNi(CO)_n^-$ (n = 3–5) at 355 nm. The photoelectron spectrum of $ZrNi(CO)_3^-$ at 532 nm is depicted in the embedded figure. The raw image (upper) and the reconstructed image (bottom) after inverse Abel transformation are shown on the left side. The double arrow indicates the direction of the laser polarization. Photoelectron spectra are shown on the right side. Vibrational progression of the ground state is indicated with vertical lines for n = 3.

The ADE value was estimated by drawing a straight line at the rising edge of the main band. The ADE values of $TiNi(CO)_n^-$ (n = 3–7) were evaluated to be 1.83 ± 0.09, 2.26 ± 0.06, 2.61 ± 0.04, 2.77 ± 0.04, and 2.72 ± 0.04 eV (Table 1), respectively.

It can be seen from Fig. 2 and 3 that the 355 nm photoelectron images and spectra of $ZrNi(CO)_n^-$ and $HfNi(CO)_n^-$ (n = 3–5) are similar to those of $TiNi(CO)_n^-$. The 532 nm spectra for $ZrNi(CO)_3^-$ and $HfNi(CO)_3^-$ are depicted in the embedded figures. The VDE values of $ZrNi(CO)_n^-$ (n = 3–5) were estimated to be 2.04 ± 0.07, 2.62 ± 0.04, and 3.01 ± 0.02 eV (Table 2), respectively. The VDE values of $HfNi(CO)_n^-$ (n = 3–5) were measured to be 2.09 ± 0.08, 2.68 ± 0.04, and 3.11 ± 0.02 eV (Table 2), respectively.

4.2 Comparison between experimental and theoretical results

Quantum chemical calculations were carried out to elucidate the geometric and electronic structures and support the spectral assignments. Optimized structures of $TiNi(CO)_n^-$ (n = 3–7) are illustrated in Fig. 4 and those of $ZrNi(CO)_n^-$ and $HfNi(CO)_n^-$ are depicted in Fig. S2 and S3 (ESI†), respectively. None of the quartet anions were found to be energetically competitive with

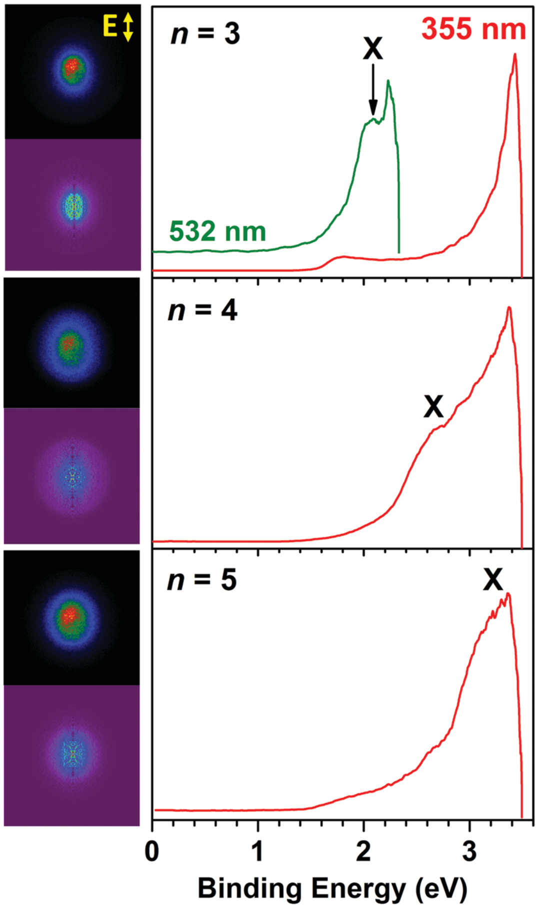

Fig. 3 Photoelectron images of $HfNi(CO)_n^-$ (n = 3–5) at 355 nm. The photoelectron spectrum of $HfNi(CO)_3^-$ at 532 nm is depicted in the embedded figure. The raw image (upper) and the reconstructed image (bottom) after inverse Abel transformation are shown on the left side. The double arrow indicates the direction of the laser polarization. Photoelectron spectra are shown on the right side.

Table 1 Comparison of experimental VDE and ADE values to BP86 calculated values of the five lowest-energy isomers for $TiNi(CO)_n^-$ (n = 3–7)

		VDE (eV)		ADE (eV)	
Cluster	Isomer	Exp.[a]	Calc.	Exp.[a]	Calc.
n = 3	3A	1.93(8)	2.18	1.83(9)	2.13
	3B		1.84		1.76
	3C		2.13		1.98
	3D		2.00		1.74
	3E		1.65		0.98
n = 4	4A	2.56(5)	2.58	2.26(6)	2.23
	4B		2.50		2.33
	4C		2.77		2.22
	4D		2.36		2.15
	4E		2.19		1.98
n = 5	5A	2.98(3)	3.10	2.61(4)	2.84
	5B		2.91		2.74
	5C		3.00		2.75
	5D		2.74		2.58
	5E		2.67		2.50
n = 6	6A	3.05(2)	3.12	2.77(4)	2.69
	6B		3.39		3.10
	6C		3.01		2.58
	6D		2.94		2.68
	6E		2.76		2.60
n = 7	7A	3.10(2)	3.17	2.72(4)	2.82
	7B		3.23		2.99
	7C		3.10		2.87
	7D		2.94		2.70
	7E		2.78		2.50

[a] Numbers in parentheses represent the uncertainty in the last digit.

Table 2 Comparison of experimental VDE and ADE values to BP86 calculated values of the most stable isomer for $MNi(CO)_n^-$ (M = Zr and Hf; n = 3–5)

		VDE (eV)		ADE (eV)	
Cluster	Isomer	Exp.[a]	Calc.	Exp.[a]	Calc.
$ZrNi(CO)_3^-$	3-I	2.04(7)	2.32	1.86(8)	2.11
$ZrNi(CO)_4^-$	4-I	2.62(4)	2.51	2.31(6)	2.15
$ZrNi(CO)_5^-$	5-I	3.01(2)	3.21	2.62(4)	2.67
$HfNi(CO)_3^-$	3-i	2.09(8)	2.24	1.91(8)	2.02
$HfNi(CO)_4^-$	4-i	2.68(4)	2.69	2.40(5)	2.44
$HfNi(CO)_5^-$	5-i	3.11(2)	3.37	2.67(4)	2.69

[a] Numbers in parentheses represent the uncertainty in the last digit.

the corresponding doublet isomers. Accordingly, only the results obtained for the representative low-energy isomers with the doublet electronic state are shown here. Tables 1 and 2 list the comparison of experimental VDE and ADE values to BP86 calculated values of the five lowest-energy isomers for $TiNi(CO)_n^-$ (n = 3–7) and the most stable isomer for $MNi(CO)_n^-$ (M = Ti, Zr, Hf; n = 3–5), respectively.

$TiNi(CO)_3^-$. In Fig. 4, the lowest-energy isomer (labeled as 3A) is a C_s structure with an $^2A'$ ground state, in which three types of coordination configurations (*i.e.*, side-on-bonded, bridging, and terminal) are simultaneously involved and the terminal CO is bonded to the Ni atom. The second isomer (3B) has three bridging CO molecules and lies higher in energy above 3A by 0.26 eV. The 3C isomer (+0.34 eV) has two bridging carbonyls and one carbonyl terminally bonded to the Ni atom. The 3D isomer (+0.37 eV) consists of one side-on-bonded carbonyl, one bridging carbonyl, and one carbonyl terminally bonded to the Ti atom. The 3E isomer (+0.99 eV) consists of one bridging carbonyl, one carbonyl terminally bonded to the Ti atom, and one carbonyl terminally bonded to the Ni atom. As listed in Table 1, the calculated VDE of 3A (2.18 eV) is consistent with experiment (1.93 ± 0.08 eV). The calculated ADE value of 3A also agrees with experiment (Table 1). The isomers 3B–3E should be too high in energy to be probed in the experiment.

$TiNi(CO)_4^-$. The lowest-energy isomer of $TiNi(CO)_4^-$ (4A) was characterized by a C_s structure with a $^2A'$ ground state, which consists of three bridging carbonyls and one terminal carbonyl bonded to the Ni atom. The 4B isomer (+0.10 eV) has one side-on-bonded carbonyl, one bridging carbonyl, and two terminal carbonyls. In 4C and 4D, the terminal carbonyl is bonded to the Ti atom, and their energies are increased by 0.36 and 0.40 eV above that of 4A, respectively. The 4E isomer could

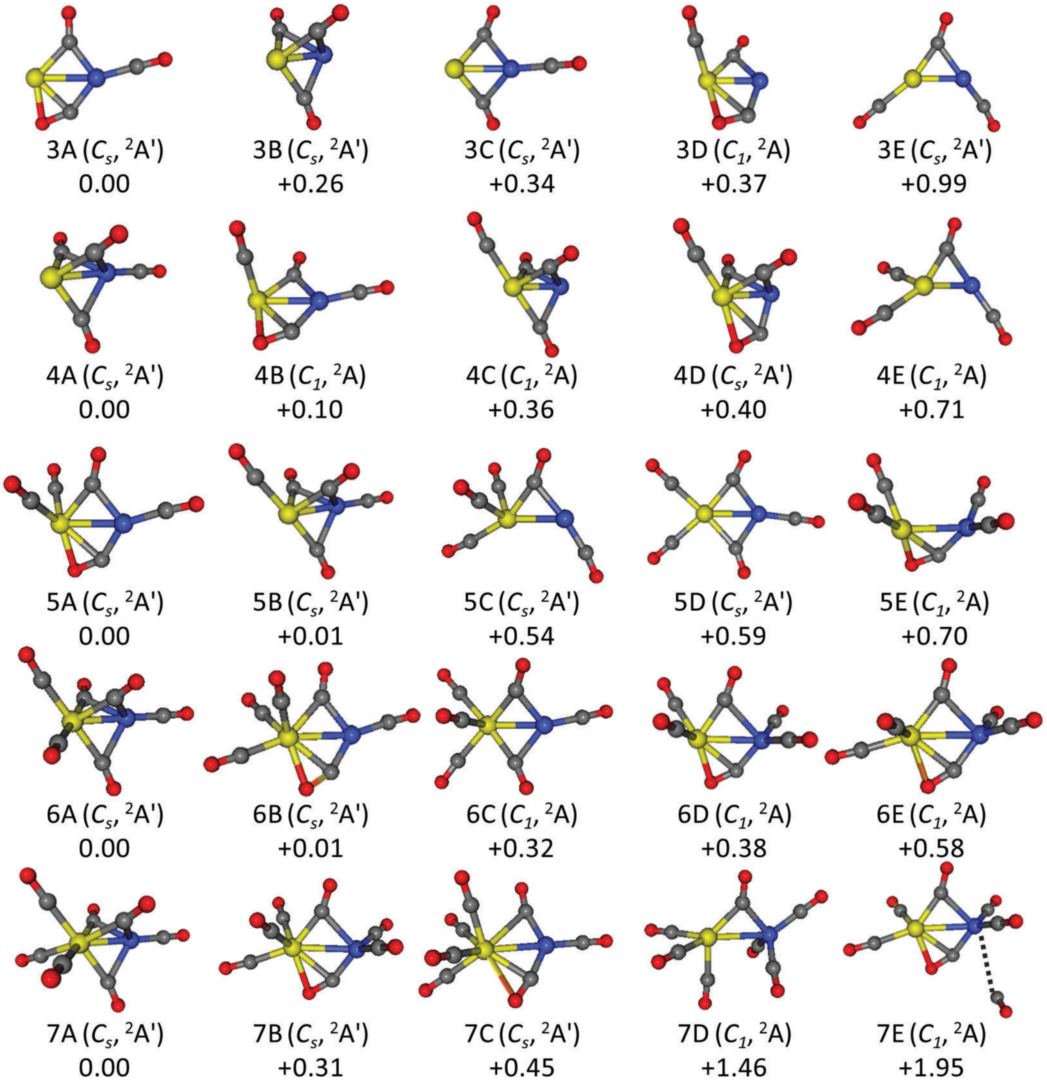

Fig. 4 Optimized structures of the five lowest-energy isomers for $TiNi(CO)_n^-$ (n = 3–7) (Ti, yellow; Ni, blue; C, gray; O, red). Relative energies are given in eV.

be viewed as being derived from 3E by terminally bonding the fourth CO molecule to the Ti atom. The calculated VDE and ADE values for the most stable structure 4A (2.58 and 2.23 eV) agree best with the experimental values of 2.56 ± 0.05 and 2.26 ± 0.06 eV (Table 1). However, the calculated VDE and ADE values of 4B (2.50 and 2.33 eV) are also close to those of experiment, indicating that the coexistence of isomers is likely here. The energetically higher-lying isomers 4C–4E could not be readily formed under the present experimental conditions, and their calculated VDE values could not fit as well with the experiment as compared to those of 4A and 4B.

$TiNi(CO)_5^-$. The lowest-energy isomer of $TiNi(CO)_5^-$ (5A) has one side-on-bonded carbonyl, one bridging carbonyl, and three terminal carbonyls, in which the two terminal carbonyls are bonded to the Ti atom and another one terminal carbonyl is bonded to the Ni atom. The second isomer (5B) consists of three bridging carbonyls, one carbonyl terminally bonded to the Ti atom, and one carbonyl terminally bonded to the Ni atom, which is only 0.01 eV above 5A. The 5C isomer (+0.54 eV) has one bridging carbonyl, three carbonyls terminally bonded to the Ti atom, and one carbonyl terminally bonded to the Ni atom. The 5D isomer (+0.59 eV) consists of two bridging carbonyls, two carbonyls terminally bonded to the Ti atom, and one carbonyl terminally bonded to the Ni atom. The 5E isomer (+0.70 eV) has one side-on-bonded carbonyl, two carbonyls terminally bonded to the Ti atom, and two carbonyls terminally bonded to the Ni atom. The VDEs of nearly energy-identical isomers 5A and 5B were predicted to be 3.10 and 2.91 eV, respectively, which are in accordance with the experiment value of 2.98 ± 0.03 eV (Table 1). The calculated ADE values of 5A and 5B are also consistent with the experimental value (2.61 ± 0.03 eV). This indicates that the isomers 5A and 5B likely coexisted. The energetically higher-lying isomers 5C–5E could not be readily generated under the present experimental conditions.

$TiNi(CO)_6^-$. In the lowest-energy isomer for $TiNi(CO)_6^-$, 6A, three carbonyls are in the bridging configuration, two carbonyls are bonded terminally to the Ti atom, and one carbonyl is bonded terminally to the Ni atom. The second isomer (6B) is only 0.01 eV above 6A and consists of one side-on-bonded carbonyl, one bridging carbonyl, three carbonyls terminally bonded to the Ti atom, and one carbonyl terminally bonded to the Ni atom. The 6C isomer (+0.32 eV) has two bridging carbonyls, three carbonyls terminally bonded to the Ti atom, and one carbonyl terminally bonded to the Ni atom. The 6D and 6E isomers consist of one side-on-bonded carbonyl, one bridging carbonyl, two carbonyls terminally bonded to the Ti atom, and two carbonyls terminally bonded to the Ni atom, and there is a slight distortion between these two structures. The calculated VDE and ADE values of 6A (3.12 and 2.69 eV) agree best with the experimental values of 3.05 ± 0.02 and 2.77 ± 0.04 eV (Table 1), whereas those for 6B (3.39 and 3.10 eV) are much higher than the experimental values. This suggests that the 6A isomer should be responsible for the $n = 6$ spectrum.

$TiNi(CO)_7^-$. The lowest-energy isomer of $TiNi(CO)_7^-$ (7A) is derived from 6A by terminally bonding the CO molecule to the Ti atom. Based on the 6B structure, the addition of the seventh CO molecule to the Ni atom results in the 7B structure, which is 0.31 eV higher above 7A. The 7C isomer (+0.45 eV) consists of one side-on-bonded carbonyl, one bridging carbonyl, four carbonyls terminally bonded to the Ti atom, and one carbonyl terminally bonded to the Ni atom. The 7D isomer (+1.46 eV) has one bridging carbonyl, three carbonyls terminally bonded to the Ti atom, and three carbonyls terminally bonded to the Ni atom. The 7E isomer (+1.95 eV) consists of one side-on-bonded carbonyl, one bridging carbonyl, two carbonyls terminally bonded to the Ti atom, two carbonyls terminally bonded to the Ni atom, and one carbonyl weakly bonded to the Ni atom. The calculated VDE and ADE values of 7A (3.10 and 2.82 eV) agree within 0.10 eV with the experimental values of 3.10 ± 0.02 and 2.72 ± 0.04 eV (Table 1). The 7B–7E isomers should be too high in energy to be detected under the present experimental conditions.

It can be seen from Fig. 4 and Fig. S2, S3 (ESI†) that the configurations of $ZrNi(CO)_n^-$ and $HfNi(CO)_n^-$ (n = 3–7) are similar to those of $TiNi(CO)_n^-$. The calculated VDE and ADE values of the most stable isomers for $ZrNi(CO)_n^-$ and $HfNi(CO)_n^-$ are in agreement with the experimental values (Table 2).

5. Discussion

The agreement between the experimental and theoretical results provides an explanation for the structure and energetics of $MNi(CO)_n^-$ (M = Ti, Zr, Hf; n = 3–7). For $TiNi(CO)_n^-$ (n = 3–7), the VDE value increases with an increase of cluster size, implying that the negative electron is stabilized upon the bonding of CO molecules. As illustrated in Fig. 5, the converged trend of the VDE value as a function of cluster size indicates that the chemisorbed carbonyls tend to be saturated around $n = 7$. The experimental VDE and ADE values of $n = 3$ are much smaller than those of n = 4–7, suggesting that the structural motif of $n = 3$ is different from that of n = 4–7. For $TiNi(CO)_3^-$, the 3A structure is favored (Fig. 4), which includes one side-on-bonded carbonyl, one bridging carbonyl, and one terminal carbonyl. Two low-lying isomers of 4A and 4B are found to be responsible for $TiNi(CO)_4^-$, which contain the $TiNi(\mu\text{-}CO)_3$ and $TiNi[\eta^2(\mu_2\text{-}C, O)](\mu\text{-}CO)$ motifs, respectively. The two nearly energy-identical isomers 5A and 5B for $TiNi(CO)_5^-$ also include the $TiNi[\eta^2(\mu_2\text{-}C, O)](\mu\text{-}CO)$ and $TiNi(\mu\text{-}CO)_3$ motifs, respectively. The 6A and 7A isomers are assigned to be the structures for $TiNi(CO)_6^-$ and $TiNi(CO)_7^-$, respectively, which are derived from 5B by terminally bonding the CO molecules to the Ti atom. In summary, three different types of CO bonding configurations (side-on-bonded, bridging, and terminal carbonyls) are successfully captured in the $n = 3$ cluster. The building block of three bridging CO molecules ($TiNi(\mu\text{-}CO)_3$) is favored at $n = 4$, the structure of which persists up to $n = 7$. The additional CO ligands are in the terminal coordination fashion. A different structural motif has also been found in the $Ti_2(CO)_n^-$ (n = 1–9) clusters, in which the building block of $Ti_2[\eta^2(\mu_2\text{-}C, O)]_3$ is favored for n = 3–5 and $Ti_2[\eta^2(\mu_2\text{-}C, O)]_2$ for n = 6–9.[25]

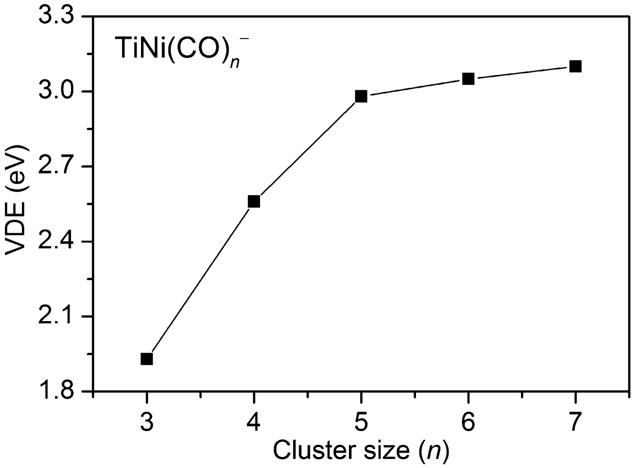

Fig. 5 The vertical detachment energy (VDE) of $TiNi(CO)_n^-$ (n = 3–7) as a function of cluster size.

The molecular orbital pictures of the most stable isomers for $TiNi(CO)_n^-$ are depicted in Fig. 6. The HOMO of 3A is a π type bond feature with prominent metal to carbonyl donation. The HOMO−1, HOMO−2, HOMO−3, and HOMO−4 are delocalized π orbitals mainly involving the metal–carbon unit. This implies that the $TiNi(CO)_3^-$ cluster is stabilized by the π orbitals localized on the interaction of CO molecules with the TiNi binuclear cluster. Similar bonding features have also been observed in the 4A–7A isomers (Fig. 6). This is reminiscent of bonding mechanism of the $M_2[\eta^2(\mu_2\text{-}C, O)]$ (M = Sc, Y, La, Ce, Gd, Ti) clusters,[34–39] in which the C–O bonding is significantly weakened.

It can be inferred from the above analysis that $TiNi(CO)_3^-$ is capable of simultaneously accommodating three different types of CO bonding (*i.e.*, side-on-bonded, bridging, and terminal modes), resulting in the formation of a $MNi[\eta^2(\mu_2\text{-}C, O)](\mu\text{-}CO)(CO)^-$ structure. This is quite different from its homobinuclear carbonyl $Ti_2(CO)_3^-$ with the involvement of three side-on-bonded CO ligands[25] and $Ni_2(CO)_3$ with the involvement of one bridging and two terminal CO ligands.[40] The CO bonding feature in $TiNi(CO)_3^-$ also holds true for $ZrNi(CO)_3^-$ and $HfNi(CO)_3^-$ (Fig. S2 and S3, ESI†), showing the similarity down through the groups

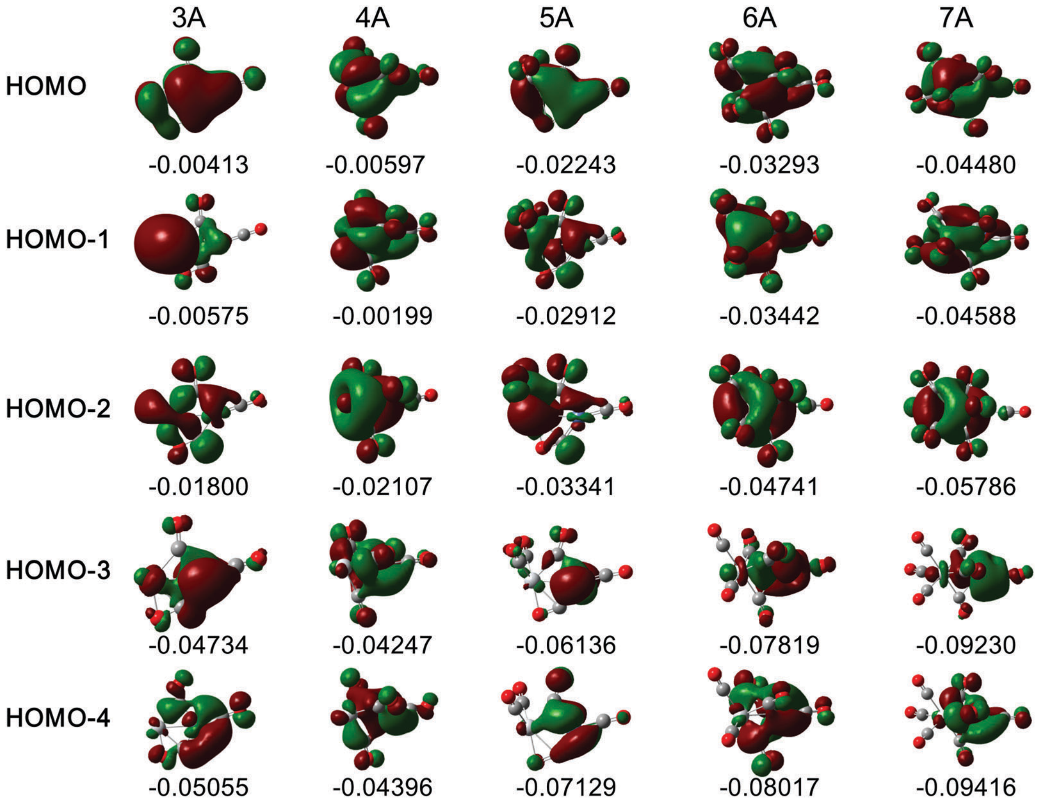

Fig. 6 Molecular orbital pictures of the most stable isomers for $TiNi(CO)_n^-$ (n = 3–7) (3A–7A), showing the highest occupied molecular orbitals down to the fourth valence molecular orbital from the HOMO.

of the periodic table. In contrast, the three carbonyls are preferentially bonded to the nickel atom in the heterobinuclear main group metal–nickel carbonyls $MNi(CO)_3^-$ (M = Mg, Ca, Al).[30] Analogously, the carbonyl groups are bonded to the nickel atom in the $CuNi(CO)_3^-$ complex[26] or the iron atom in the $CuFe(CO)_4^-$ and $PbFe(CO)_4^-$ clusters.[27,28] In $TiNi(CO)_3^-$, the C–O bond distance in the side-on-bonded, bridging, and terminal motion was calculated to be about 1.29, 1.21, and 1.18 Å, respectively, which is longer than that of the free CO molecule (1.13 Å). The CO stretching frequency of the individual side-on-bonded, bridging, and terminal carbonyl group in $TiNi(CO)_3^-$ was predicted to be 1323, 1658, and 1905 cm^{-1} (unscaled), respectively, pointing to the extreme, moderate, and weak C–O bond activation. Interestingly, the anomalous C–O bond weakening has been reported for chemisorbed CO in side-on-bonded modes on transition metal surfaces as model catalysts, for which the ν_{C-O} values are observed around 1100–1400 cm^{-1}.[4–6] The bridging and terminal bonding of CO on metal catalyst is a common feature. Then, the $MNi[\eta^2(\mu_2\text{-C,O})](\mu\text{-CO})(CO)^-$ (M = Ti, Zr, Hf) complexes represent almost all the main modes of metal–CO coordination to date. This interesting tricarbonyl model would be expected to work for $MNi(CO)_3^-$ (M = Sc, Y, La, Ce; or the other early transition metals). These findings would have important implications for understanding the chemisorbed CO molecules on metal catalysts and adjusting the appropriate CO activation *via* the selection of different transition metals.

6. Conclusions

The chemical bonding and electronic structure of heteronuclear group 4 metal–nickel clusters $MNi(CO)_n^-$ (M = Ti, Zr, Hf; n = 3–7) have been investigated by mass-selected photoelectron velocity-map imaging spectroscopy and quantum chemical calculations. Three different types of CO bonding configurations (side-on-bonded, bridging, and terminal carbonyls) are simultaneously involved in the n = 3 cluster, which serves as a new example of the smallest metal carbonyl with the involvement of all the main modes of metal–CO coordination to date. The building block of three bridging CO molecules is favored at n = 4, the structure of which persists up to n = 7. The additional CO ligands are in the terminal coordination mode in the larger clusters. The present findings would advance the understanding of CO binding on metal surfaces.

Acknowledgements

This study was supported by the National Natural Science Foundation of China (Grant No. 21327901, 21473193, 21503222, and 21673231), the Key Research Program (Grant No. KGZD-EW-T05), and the Strategic Priority Research Program (Grant No. XDB17010000) of the Chinese Academy of Science. L. J. acknowledges the Hundred Talents Program of Chinese Academy of Sciences.

References

1 F. A. Cotton, G. Wilkinson, C. A. Murillo and M. Bochmann, *Advanced inorganic chemistry*, John Wiley & Sons, New York, 1999.

2 R. Schlogl and S. B. Abd Hamid, *Angew. Chem., Int. Ed.*, 2004, **43**, 1628–1637.

3 H. J. Freund, G. Meijer, M. Scheffler, R. Schlogl and M. Wolf, *Angew. Chem., Int. Ed.*, 2011, **50**, 10064–10094.

4 F. M. Hoffmann and R. A. Depaola, *Phys. Rev. Lett.*, 1984, **52**, 1697–1700.

5 N. D. Shinn and T. E. Madey, *Phys. Rev. Lett.*, 1984, **53**, 2481–2484.

6 D. W. Moon, S. L. Bernasek, D. J. Dwyer and J. L. Gland, *J. Am. Chem. Soc.*, 1985, **107**, 4363–4364.

7 F. A. Cotton, B. A. Frenz and L. Kruczyns, *J. Am. Chem. Soc.*, 1973, **95**, 951–952.

8 R. Colton and M. J. McCormick, *Coord. Chem. Rev.*, 1980, **31**, 1–52.

9 W. A. Herrmann, H. Biersack, M. L. Ziegler, K. Weidenhammer, R. Siegel and D. Rehder, *J. Am. Chem. Soc.*, 1981, **103**, 1692–1699.

10 A. J. Bridgeman, *Inorg. Chim. Acta*, 2001, **321**, 27–41.

11 M. F. Zhou, L. Andrews and C. W. Bauschlicher, *Chem. Rev.*, 2001, **101**, 1931–1961.

12 Q. Xu, *Coord. Chem. Rev.*, 2002, **231**, 83–108.

13 A. Fielicke, P. Gruene, G. Meijer and D. M. Rayner, *Surf. Sci.*, 2009, **603**, 1427–1433.

14 A. M. Ricks, Z. E. Reed and M. A. Duncan, *J. Mol. Spectrosc.*, 2011, **266**, 63–74.

15 E. F. van der Eide, G.-L. Hou, S. H. M. Deng, H. Wen, P. Yang, R. M. Bullock and X.-B. Wang, *Organometallics*, 2013, **32**, 2084–2091.

16 J. M. Cui, X. J. Zhou, G. J. Wang, C. X. Chi, Z. P. Liu and M. F. Zhou, *J. Phys. Chem. A*, 2013, **117**, 7810–7817.

17 H. J. Zhai, B. Kiran, B. Dai, J. Li and L. S. Wang, *J. Am. Chem. Soc.*, 2005, **127**, 12098–12106.

18 G. S. IckingKonert, H. Handschuh, G. Gantefor and W. Eberhardt, *Phys. Rev. Lett.*, 1996, **76**, 1047–1050.

19 J. M. Cui, X. J. Zhou, G. J. Wang, C. X. Chi, Z. H. Li and M. F. Zhou, *J. Phys. Chem. A*, 2014, **118**, 2719–2727.

20 I. Swart, F. M. F. de Groot, B. M. Weckhuysen, D. M. Rayner, G. Meijer and A. Fielicke, *J. Am. Chem. Soc.*, 2008, **130**, 2126–2127.

21 D. T. Moore, J. Oomens, J. R. Eyler, G. Meijer, G. von Helden and D. P. Ridge, *J. Am. Chem. Soc.*, 2004, **126**, 14726–14727.

22 C. X. Chi, J. M. Cui, Z. H. Li, X. P. Xing, G. J. Wang and M. F. Zhou, *Chem. Sci.*, 2012, **3**, 1698–1706.

23 G. J. Wang, J. M. Cui, C. X. Chi, X. J. Zhou, Z. H. Li, X. P. Xing and M. F. Zhou, *Chem. Sci.*, 2012, **3**, 3272–3279.

24 X. J. Zhou, J. M. Cui, Z. H. Li, G. J. Wang and M. F. Zhou, *J. Phys. Chem. A*, 2012, **116**, 12349–12356.

25 J. H. Zou, H. Xie, D. X. Dai, Z. C. Tang and L. Jiang, *J. Chem. Phys.*, 2016, **145**, 184302.

26 Z. L. Liu, H. Xie, Z. B. Qin, H. J. Fan and Z. C. Tang, *Inorg. Chem.*, 2014, **53**, 10909–10916.

27 N. Zhang, M. B. Luo, C. X. Chi, G. J. Wang, J. M. Cui and M. F. Zhou, *J. Phys. Chem. A*, 2015, **119**, 4142–4150.

28 Z. L. Liu, J. H. Zou, Z. B. Qin, H. Xie, H. J. Fan and Z. C. Tang, *J. Phys. Chem. A*, 2016, **120**, 3533–3538.

29 H. Qu, F. C. Kong, G. J. Wang and M. F. Zhou, *J. Phys. Chem. A*, 2016, **120**, 7287–7293.

30 H. Xie, J. H. Zou, Q. Q. Yuan, H. J. Fan, Z. C. Tang and L. Jiang, *J. Chem. Phys.*, 2016, **144**, 124303.

31 Z. B. Qin, X. Wu and Z. C. Tang, *Rev. Sci. Instrum.*, 2013, **84**, 066108.

32 M. J. Frisch, G. W. Trucks, H. B. Schlegel, G. E. Scuseria, M. A. Robb, J. R. Cheeseman, G. Scalmani, V. Barone, B. Mennucci, G. A. Petersson, H. Nakatsuji, M. Caricato, X. Li, H. P. Hratchian, A. F. Izmaylov, J. Bloino, G. Zheng, J. L. Sonnenberg, M. Hada, M. Ehara, K. Toyota, R. Fukuda, J. Hasegawa, M. Ishida, T. Nakajima, Y. Honda, O. Kitao, H. Nakai, T. Vreven, J. A. Montgomery Jr., J. E. Peralta, F. Ogliaro, M. J. Bearpark, J. Heyd, E. N. Brothers, K. N. Kudin, V. N. Staroverov, R. Kobayashi, J. Normand, K. Raghavachari, A. P. Rendell, J. C. Burant, S. S. Iyengar, J. Tomasi, M. Cossi, N. Rega, N. J. Millam, M. Klene, J. E. Knox, J. B. Cross, V. Bakken, C. Adamo, J. Jaramillo, R. Gomperts, R. E. Stratmann, O. Yazyev, A. J. Austin, R. Cammi, C. Pomelli, J. W. Ochterski, R. L. Martin, K. Morokuma, V. G. Zakrzewski, G. A. Voth, P. Salvador, J. J. Dannenberg, S. Dapprich, A. D. Daniels, O. Farkas, J. B. Foresman, J. V. Ortiz, J. Cioslowski and D. J. Fox, *Gaussian 09*, Gaussian, Inc., Wallingford, CT, USA, 2009.

33 Q. Luo, Q. S. Li, Z. H. Yu, Y. M. Xie, R. B. King and H. F. Schaefer, *J. Am. Chem. Soc.*, 2008, **130**, 7756–7765.

34 L. Jiang and Q. Xu, *J. Am. Chem. Soc.*, 2005, **127**, 42–43.

35 Q. Xu, L. Jiang and N. Tsumori, *Angew. Chem., Int. Ed.*, 2005, **44**, 4338–4342.

36 L. Jiang and Q. Xu, *J. Phys. Chem. A*, 2006, **110**, 5636–5641.

37 X. Jin, L. Jiang, Q. Xu and M. F. Zhou, *J. Phys. Chem. A*, 2006, **110**, 12585–12591.

38 Q. Xu, L. Jiang and R. Q. Zou, *Chem. – Eur. J.*, 2006, **12**, 3226–3232.

39 M. F. Zhou, X. Jin and J. Li, *J. Phys. Chem. A*, 2006, **110**, 10206–10211.

40 I. S. Ignatyev, H. F. Schaefer, R. B. King and S. T. Brown, *J. Am. Chem. Soc.*, 2000, **122**, 1989–1994.